12th International Symposium on Turbulence and Shear Flow Phenomena (TSFP12)
Osaka, Japan (Online), July 19-22, 2022

DRAG REDUCTION ON A TRANSONIC AIRFOIL

Maurizio Quadrio
Dipartimento di Scienze e Tecnologie Aerospaziali
Politecnico di Milano
via La Masa 34, 20156 Milano, Italy
maurizio.quadrio@polimi.it

Alessandro Chiarini
Dipartimento di Scienze e Tecnologie Aerospaziali
Politecnico di Milano
via La Masa 34, 20156 Milano, Italy
alessandro.chiarini@polimi.it

Jacopo Banchetti
Dipartimento di Scienze e Tecnologie Aerospaziali
Politecnico di Milano
via La Masa 34, 20156 Milano, Italy
jacopo.banchetti@polimi.it

Davide Gatti
Institute for Fluid Mechanics
Karlsruhe Institute of Technology
Kaiserstr. 10, 76131 Karlsruhe, Germany
davide.gatti@kit.edu

Antonio Memmolo
High Performance Computing Department
CINECA-Interuniv. Cons., 40033 Bologna, Italy
antonio.memmolo@cineca.it

Sergio Pirozzoli
Dipartimento di Ingegneria Meccanica e Aerospaziale,
Sapienza Univ. Roma, Via Eudossiana, Roma, Italy
sergio.pirozzoli@uniroma1.it

Abstract

Flow control for reducing skin-friction drag in the turbulent regime is applied to a transonic airfoil to improve its global aerodynamic performance. The study relies on direct numerical simulations of the compressible turbulent flow around a supercritical airfoil at Reynolds and Mach numbers of $Re_\infty = 3 \times 10^5$ and $M_\infty = 0.7$. The control is applied on a portion of the airfoil suction side only. However, besides locally reducing drag, the control modifies the position and the intensity of the shock wave and significantly improves the aerodynamic efficiency of the airfoil by increasing the lift and slightly decreasing the total drag. The increase of the aerodynamic efficiency implies that the airfoil can achieve the desired lift at a lower angle of attack and, therefore, with a much lower drag. Estimates of the benefits on a full aircraft are provided and indicate that substantial savings are possible, even when the energy cost of an active control is considered. These results suggest that skin-friction drag reduction should no be considered as a goal only, but also as tool to modify and control the global aerodynamics of complex flows.

Introduction

Flow control for reducing turbulent skin-friction drag has arouse the interest of scholars over the years, because of efficiency and environmental reasons. However, to date only few strategies have been deployed in applications, owing to an often critical cost/benefit ratio. Most research for skin-friction drag reduction has taken place in parallel flows, where drag is entirely due to friction. Unfortunately, friction drag reduction of both passive (e.g. riblets) and active techniques (e.g. spanwise forcing) are proportional to the portion of the surface covered by the drag-reducing device.

In more complex flows the aerodynamic drag contains additional contributions besides the viscous friction, such as pressure drag, parasitic drag, separation, lift-induced drag and wave drag, and what ultimately matters is reducing the overall drag and not only the friction contribution. Only over the last years some researchers have begun considering how the reduction of turbulent skin-friction affects the other drag contributions. For example Banchetti *et al.* (2020) applied stramwise traveling waves of spanwise forcing (Quadrio *et al.*, 2009) on the incompressible turbulent flow past a bump to investigate the effect of skin-friction reduction on pressure drag. They found that a distributed reduction of friction influences the pressure field largely reducing the associated drag contribution, increasing by one half the net energetic benefits. Later Nguyen *et al.* (2021) studied the effect of a temporally spanwise-oscillating pressure gradient in a channel flow with transverse bars at the wall. They observed that pressure drag is reduced almost as the friction drag, but that in this case the net energy budget remains slightly negative.

The airplane is one of the applications where flow control mat play a key role. Here the goal is not a decrease of the drag only, but the enhancement of the lift/drag ratio, i.e. the aerodynamic efficiency. Recently Atzori *et al.* (2020) used high-fidelity incompressible Large Eddy Simulations to study the effect of uniform blowing and suction on a NACA4412 airfoil at a Reynolds number based on free-stream velocity and chord length of $Re = 200,000$ and observed an increase of the aerodynamic efficiency up to 11%. Albers & Schröder (2021) considered the same airfoil and the same Re, but controlled the flow with spanwise travelling waves of wall-normal deformation. As in their previous work based on a different airfoil, they found that the control favourably modifies both the friction and pressure drag, yielding a global increase of the aerodynamic performances. Similarly, Kornilov (2021) estimated a net power saving up to 8% for a NACA0012 airfoil controlled

with low-amplitude blowing/suction.

All the above mentioned works have considered the flow in incompressible or subsonic regime. However, following the work by Mele *et al.* (2016) there are reasons to suspect that a further advantage of reducing skin friction resides in the ability to interact with the position and the strength of the shock wave generated over a wing in the transonic regime. Since civil aircraft cruise and military aircraft maneuver in the transonic regime, this would be of paramount importance in assessing the effectiveness of flow control for aeronautical applications. Unfortunately, reliable simulations of the flow over a transonic airfoil with flow control for skin-friction drag reduction are less widespread. In this work we present the first direct numerical simulation (DNS) of the compressible turbulent flow over an airfoil in the transonic regime, where flow control for skin-friction reduction is applied. We explore to what extent a localised control for skin-friction reduction alters the aerodynamic performances of the airfoil. The results are also extrapolated to the entire airplane to provide an estimate of the potential savings.

Methods

We investigate the transonic flow around the V2C airfoil, a supercritical airfoil designed by Dassault Aviation in the context of the European research program TFAST. The Reynolds and Mach numbers of the flow are set to $Re_\infty = U_\infty c/\nu_\infty = 3\times10^5$ and $M_\infty = U_\infty/a_\infty = 0.7$; c is the airfoil chord and U_∞, ν_∞ and a_∞ are the free-stream velocity, kinematic viscosity and sound speed. The angle of attack is $\alpha = 4\,\mathrm{deg}$, which corresponds to the maximum aerodynamic efficiency of the profile at this Re_∞ and M_∞. The DNS code (Memmolo *et al.*, 2018) solves the compressible Navier–Stokes equations for a calorically perfect gas and is based on a second-order finite volume method, which switches to third-order WENO scheme using a modified Ducros sensor (Ducros *et al.*, 1999). Time advancement is carried out with the low-storage, third-order Runge–Kutta scheme. At the farfield, characteristics-based non-reflective boundary conditions are used (Poinsot & Lele, 1992), while periodicity is enforced in the spanwise direction. A C-type mesh with radius of $25c$ is employed, with the outflow placed at $25c$ from the trailing edge. The domain extends for $0.1c$ in the spanwise z direction which is enough to ensure decorrelation of all the flow structures (Zhang & Samtaney, 2016; Hosseini *et al.*, 2016). The incoming flow is laminar and, following Schlatter & Örlü (2012), the transition to turbulence is enforced at $x = x_f = 0.1c$ via a volume force (tripping) on both sides of the airfoil.

The streamwise-travelling waves of spanwise velocity (Quadrio *et al.*, 2009) are applied on a fraction of the suction side of the airfoil only. The spanwise component of the velocity at the wall w_w enforced by the control is:

$$w_w(x,t) = f(x)A\sin(\kappa_x x - \omega t); \tag{1}$$

A is the maximum forcing amplitude, κ_x and ω are the spatial and temporal frequencies and $f(x)$ is a smoothing function (Yudhistira & Skote, 2011). In this work, two forcing configurations are considered, hereinafter referred to as C1 and C2, corresponding to different forcing strengths. In both cases the controlled portion of the suction side starts after the tripping and extends downstream the shock wave. For C1 the actuated region extends for $0.3c \le x \le 0.78c$ and $A = 0.5$, $\omega = 11.3$ and $\kappa_x = 161$. For C2, instead, the actuated region is longer as it extends for $0.2c \le x \le 0.78c$ and the forcing amplitude is larger, i.e. $A = 0.684$. Note that in viscous units for C2 these parameters correspond to $A^+ \approx 6.6$, $\omega^+ \approx 0.06$ and $\kappa_x^+ \approx 0.013$ that is not far from the optimum for the incompressible channel flow at a friction Reynolds number of $Re_\tau = 200$.

Four DNS simulations have been carried out for the no-control, C1 and C2 cases using the baseline grid (as shown in the following the simulation dealing with C2 has also been repeated at a different angle of attack). Two further simulations for the no-control and C2 cases have been carried out on a finer grid for validation purpose. The baseline grid consists in $Nx\times Ny\times Nz = 4096\times512\times256$ points (≈ 536 millions of points) with an uniform distribution in the spanwise direction and a hyperbolic distribution in the tangential and wall normal directions to increase the resolution close to the airfoil and in the wake. The finer grid is obtained by increasing the number of points of a 1.5 factor in the three directions, yielding $N_x\times N_y\times N_z = 6144\times768\times384$, corresponding to approximately 1.8 billions of points. As verified with an a posteriori check, at the wall the requirements of $\Delta x^+ < 10$, $\Delta y^+ \le 0.5$ and $\Delta z^+ < 5$ for a fully resolved DNS (Hosseini *et al.*, 2016) are satisfied. The time step of the simulations is kept constant, i.e. $\Delta t = 1.5\times10^{-4}$ and $\Delta t = 1\times10^{-4}$ for the baseline and fine grid respectively, and has been chosen to maintain the maximum Courant-Friedrichs-Lewy number below unity. After reaching statistical equilibrium the simulations are advanced for further $40c/U_\infty$ to accumulate the flow statistics. Hereinafter all quantities are made dimensionless with c and with the free stream values.

Results

Instantaneous and mean fields

Figure 1 characterises the mean and instantaneous fields. The isosurfaces of the imaginary part λ_{ci} of the complex conjugate eigenvalues pair of the velocity gradient tensor ($\Im(\lambda_{ci} = 100$) are used to visualise the vortical structures of the uncontrolled case. The background colour map is for the Mach number of the uncontrolled case, while the three lines denote the mean sonic line $M = 1$ for the non-control (red), C1 (blue) and C2 (green) cases. The flow becomes immediately supersonic at the leading-edge of the airfoil and is laminar up to $x = 0.1$ where the tripping is applied. The flow remains supersonic up to $x \approx 0.5$, where it is abruptly recompressed by the shock wave. As detailed by the sonic lines, the forcing moves the shock wave downstream delaying the recompression and enlarging the supersonic region. The streamwise and vertical dimensions of the bubble increase from $D_x = 0.475$ and $D_y = 0.355$ for the non-control case to $D_x = 0.485$ and $D_y = 0.365$ for C1 and to $D_x = 0.516$ and $D_y = 0.425$ for C2. The downstream shift of the shock wave is accompanied by an increase of its intensity. To be quantitative, the pressure jump across the shock at $y = 0.2$ increases from $\Delta p = 0.1205$ for the non-control case to $\Delta p = 0.1363$ and $\Delta p = 0.1673$ for C1 and C2. Consistently with the enlargement of the supersonic region the maximum Mach number increases from $M = 1.087$ for the non-control case to $M = 1.093$ for C1 and $M = 1.116$ for C2. Overall, these changes are consistent with a decreased friction in the actuated region, that leads to an increase of the supersonic flow speed.

Figure 2 visualises the effect of the control on the boundary layer developing over the suction side of the airfoil. The instantaneous velocity components is plotted over a curved surface at the first grid point off the wall, i.e. $y \approx 3\times10^{-5}$,

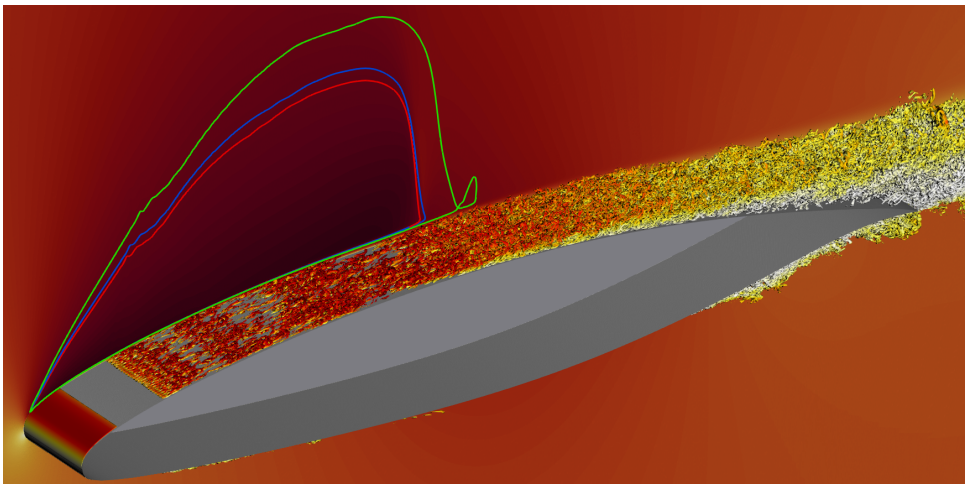

Figure 1. Isosurfaces of the swirling strength $\Im(\lambda_{ci}) = 100$ in the no-control case, coloured with the kinetic energy k with a white-to-red colormap in the range $0 \leq k \leq 1$. The background colour map is for the mean Mach number in the range. Lines are the sonic line $M = 1$ for reference (red), C1 (blue) and C2 (green).

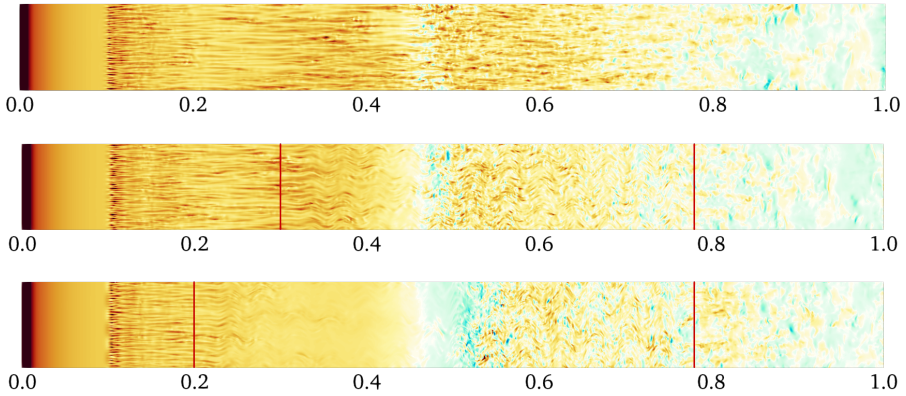

Figure 2. Instantaneous streamwise velocity component at the first grid point off the wall over the suction side, for no-control (top), C1 (middle) and C2 (bottom). The symmetric blue-to-red clourmap is for $-0.1 \leq u \leq 0.1$; the blue colour is for negative values and the red colour for positive values. The red lines mark the boundaries of the actuated region.

as a proxy of the wall friction. A pattern of alternating low- and high-speed streaks suddenly appears at $x = 0.1$ where the tripping is applied. In the non-control case the intensity of the fluctuations decreases at $x \approx 0.46$, due to the interaction of the boundary layer with the shock wave, before increasing again. The control clearly produces spanwise oscillations in the developing streaks. A decrease of the intensity of the fluctuations indicates that the control strategy is effective in reducing skin-friction. For C2 the streaks almost disappear at $x \approx 0.3$ indicating that the flow almost relaminarise before the shock wave. After the shock wave ($x \approx 0.5$) few spots with negative $u < 0$ are observed for the uncontrolled case. For the controlled cases, instead, the local backflow after the shock is more intense, in particular for C2, indicating that due to the interaction with the shock wave the boundary layer separates and gives origin to a small recirculating region.

Wall friction and pressure

The mean friction and pressure coefficients, c_f and c_p, are shown in figure 3. They are defined as

$$c_f(x) = \frac{2\tau_w(x)}{\rho_\infty U_\infty^2}, \quad c_p = \frac{2(p_w(x) - p_\infty)}{\rho_\infty U_\infty^2} \tag{2}$$

where $p_w(x)$ is the mean wall pressure and $\tau_w = \mu \hat{\boldsymbol{t}} \cdot \partial \boldsymbol{u} / \partial n|_w$ is the mean viscous stress at the wall; here $\hat{\boldsymbol{t}}$ is the tangential unit vector, μ is the dynamic viscosity and $\partial / \partial n$ denotes the wall-normal derivative. The lines refer to the simulations carried out with the baseline grid, while the symbols are for the results computed with the finer grid for the non-control and C2 cases. The results from the two grids are perfectly overlapping for the pressure coefficient. For the friction coefficient, instead, the results indicate that the baseline grid is slightly under-resolved at the leading edge. This suggest that the usual requirements for fully-resolved DNS based on the cell spacing in viscous units (Hosseini *et al.*, 2016) are not adequate. Note, however, that the changes between the uncontrolled and the controlled cases obtained with the baseline grid are well validated by the finer grid. In the following the focus is on the suction side only as the changes on the pressure side, where there is no actuation, are marginal.

After the peak at the leading-edge, the friction coefficient quickly decreases in the laminar boundary layer up to $x \approx 0.1$ where the trace of the tripping is visible. Moving downstream, the friction coefficient slowly increases before decreasing because of the shock-wave/boundary-layer interaction. For the non-control case the local maximum of c_f occurs at $x \approx 0.42$, while the local minimum is observed at $x \approx 0.47$. Downstream

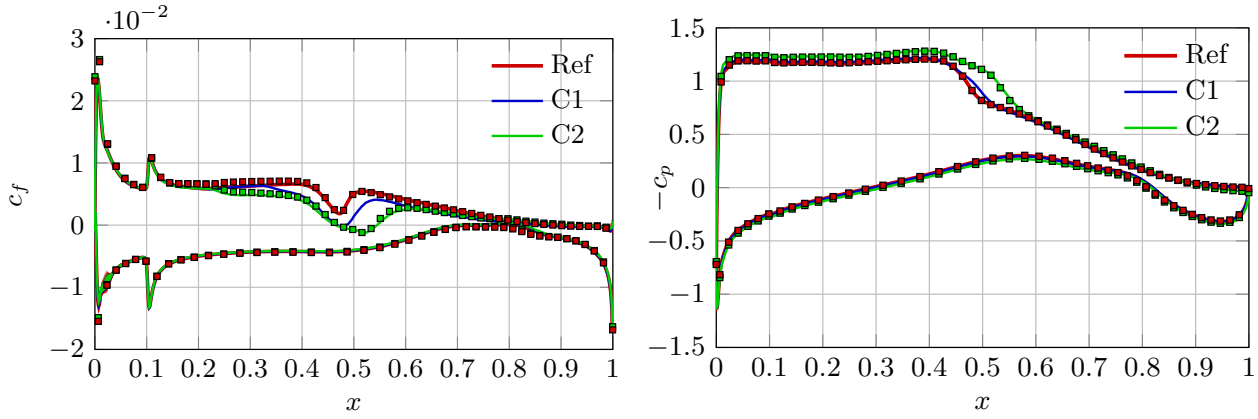

Figure 3. Friction coefficient c_f (left) and pressure coefficient c_p (right). Reference and C2 results obtained on the finer grid are shown with symbols. In the pressure side the green symbols are not visible as they are covered by the red ones.

the shock wave, after a partial recovery, c_f slowly decreases due to the mild adverse pressure gradient to eventually become negative just before the trailing edge where the flow separates. In the non-control case, although small backflow regions were detected in the instantaneous field in figure 2, the c_f remains positive just after the shock wave, indicating the absence of a mean recirculating region. In the controlled cases the spanwise forcing is effective in reducing friction in the actuated portion on the surface. As expected a short spatial transient is observed where drag reduction develops (Quadrio & Ricco, 2004; Skote, 2012). Consistently with the visualisations in figure 2, for both C1 and C2 the combined action of the control and of the SBLI lead to negative c_f after the shock wave, denoting a mean backflow region that extends for $0.46 \leq x \leq 0.49$ for C1 and for $0.46 \leq x \leq 0.54$ for the stronger C2 forcing. A final remark deals with the position of the local minimum of c_f immediately downstream the shock wave. The position of the local c_f minimum follows the downstream shift of the shock wave: it is placed at $x = 47$, 0.48 and 0.51 for the non-control, C1 and C2 cases respectively.

We now consider the pressure coefficient. After the sharp expansion at the leading-edge, c_p features a flat plateau that extends down to the shock compression. Moving further downstream, the pressure coefficient progressively increases and at the trailing edge $c_p = 0$. Unlike c_f, the control action modifies the pressure even outside the actuated region. In particular, two distinct effects are observed to modify the c_p distribution, both leading to an increase of the suction. (i) The compression associated with the shock wave is delayed. (ii) The expansion at the leading edge is more intense leading to a plateau with lower c_p. The presence of the recirculating region in the controlled cases, indeed, mitigates the adverse pressure gradient in the area close to the shock (see the milder slope of $-c_p$ in correspondence of the pressure recovery before the shock-induced compression). As a result, the shock wave moves downstream and enlarges the supersonic bubble. This leads to an increase of the velocity within the bubble and, therefore, to a more intense expansion in the fore part of the airfoil. Both these effects are more evident in the C2 controlled case, that has been designed on purpose to produce an evident recirculation after the shock wave. In a certain way, the effect of the control on c_p can be assimilated to that of a slight increase of the free-stream Mach number, but on the suction side only.

Aerodynamic forces and extrapolation

The control-induced changes of the pressure and friction distributions positively affect lift and drag. Table 1 compares the lift and drag coefficients for the uncontrolled and controlled cases; the Δ_1 and Δ_2 columns show the control-induced relative changes for $C1$ and $C2$ respectively. The friction and pressure contributions to the total drag are computed separately and reported as $C_{d,f}$ and $C_{d,p}$. For C1 and C2 the control reduces the friction drag by 7.2% and 13.4%, that are very large numbers considering that the forcing is applies only on a limited portion of the suction side. The effect of the control on the pressure drag is different in the two cases. Indeed, $C_{d,p}$ decreases by a relative 2.4% for C1 and increases by a relative 5.5% for C2. Note, however, that the combination of the friction and pressure contributions leads to an overall drag reduction for both controlled cases: for C1 C_d decreases by a relative 4.5%, while for C2 by a relative 0.8%. However, an additional favourable effect of the control is the increase of the lift coefficient. For $C1$ the increase of C_ℓ is marginal (+1.5%), as detailed by the small changes in the pressure distribution shown in figure 3. For C2, instead, the pressure distribution is largely modified and C_ℓ significantly increases by a relative 11.3%. Overall, the control leads to an increase the aerodynamic efficiency of the airfoil in both cases, quantified by 6.8% for C1 and 13.5% for C2.

An increase of the aerodynamics efficiency implies that the required lift can be obtained at the cost of a lower drag. In other words, when comparing the uncontrolled and controlled cases at constant lift coefficient, the above described control-induced increase of the lift turns into a reduction of the angle of attack and, therefore, of the total drag. To estimate the achievable ΔC_d we have computed the $C_\ell - \alpha$ and $C_d - \alpha$ maps for the uncontrolled case with auxiliary RANS simulations (not shown) carried out with a modified version of the same code used for the DNS and using the Spalart-Allmaras turbolence model. In the following only the C2 case is considered for conciseness. By assuming in first approximation that the control-induced relative changes of the aerodynamic forces remain constant for small changes of α, we estimate that for C2 the angle of attack that leads to the reference lift is $\alpha = 3.45\,\text{deg}$. A further DNS simulation has been carried out for these parameters to evaluate the control performances. As shown in the last columns of table 1 the resulting lift coefficient is $C_\ell = 0.730$ (slightly less than expected), but the drag coefficient decreases to $C_d = 0.0210$, corresponding to a relative 15% of drag reduction.

Table 1. Lift and drag coefficients (C_l, C_d) of the airfoil, and splitting of drag coefficient into friction and pressure contributions ($C_{d,f}$, $C_{d,p}$), for uncontrolled, C1 and C2 flow cases. Δ stands for relative change, and the last two columns refer to the C2 case computed for an angle of attack $\alpha = 3.45^\circ$ (see text).

	Uncontrolled	C1	Δ_1	C2	Δ_2	C2 ($\alpha = 3.45^\circ$)	Δ_2
C_l	0.740	0.751	+1.5%	0.825	+11.3%	0.730	-1.3%
C_d	0.0247	0.0236	-4.5%	0.0245	-0.8%	0.0210	-15.0%
$C_{d,f}$	0.0082	0.0076	-7.3%	0.0071	-13.4%	0.0074	-9.7%
$C_{d,p}$	0.0165	0.0161	-2.4%	0.0174	+5.5%	0.0136	-17.6
C_l/C_d	29.7	31.7	+6.8%	33.7	+13.5%	34.8	+17.2%

These benefits can be tentatively scaled up to the full aircraft to estimate the potential power savings in aeronautical applications. We consider the wing-body configurration DLR-F6 defined in the second AIAA CFD prediction workshop (Laflin *et al.*, 2005), with reference flight conditions $M_\infty = 0.75$ and $Re_\infty = 3 \times 10^6$. The reference lift coefficient is $C_L = 0.5$ that is obtained at an angle of attack of $\alpha = 0.52$ deg at the cost of $C_D = 0.0295$. In the following we try to estimate the achievable drag reduction when the more effective C2 control is applied on the wings. Because of the limited available data, the following assumptions are made: (i) the wing is responsible for the entire lift of the aircraft and, excluding the lift-induced drag contribution, for 1/3 of the total drag; (ii) the control-induced changes of C_ℓ and C_d do not vary along the wing span and do not change with α, M_∞ and Re_∞, so that the values reported in Table 1 are used. Following the same line of reasoning as for the airfoil and using the $C_L - \alpha$ and $C_D - \alpha$ maps available in `https://aiaa-dpw.larc.nasa.gov/Workshop2/DPW_forces_WB_375` we estimate that applying the C2 control on the wings, the reference C_L is obtained at an angle of attack of $\alpha = 0.0125$ deg at the cost of a total drag of $C_D = 0.0272$, corresponding to a drag reduction of approximately 8.5%. The additional small benefit of the direct skin-friction reduction leads to about 9% of total drag reduction for the entire aircraft. Also the actuation power is considered. Under the idealised assumption of actuation with unitary efficiency, it is equal to the power transferred to the viscous fluid by the boundary forcing. Using the DNS data, for the time-average actuation power we have measured $5.5 \times 10^{-4} \rho_\infty U_\infty$. As a result, because of the localised actuation area (it is approximately $1/4$ of the wing surface and $1/12$ of the aircraft surface) the actuation power is estimated to be about 1% of the overall power expenditure of the aircraft.

Concluding discussion

In this work we present the first DNS of the compressible flow turbulent flow over an airfoil in the transonic regime at $M_\infty = 0.7$ and $Re_\infty = 3 \times 10^5$, where the aerodynamic performances are enhanced by locally reducing skin friction via active spanwise forcing. The present results clearly demonstrate that in complex flows the control effects go well beyond the local reduction of skin friction. Therefore, we suggest that skin-friction drag reduction should not be considered as a goal only, but also as a tool to improve the global aerodynamic performances.

The control has been applied on a fraction of the suction side of the airfoil. Besides locally reducing skin-friction it modifies the position and the strength of the shock wave, resulting into an increase of the lift and into a decrease of the drag. Overall, this yields an enhancement of the aerodynamic efficiency. In the most effective considered control, the lift increases by a relative 11.3%, while the total drag decreases by a marginal 0.8%, corresponding to an increase of the aerodynamic efficiency of 13.5%. An increase of the aerodynamic efficiency means that in the controlled case the required lift is achieved at a lower angle of attack and, therefore, with a significant reduction of the total drag. We have measured that this leads to a total drag reduction of 15%. Scaling these results to the entire aircraft we have estimated that, in reference flight conditions, this may lead to a total drag reduction of about 8.5%. The fact that control can be applied locally to achieve a large, global benefit is of paramount importance for practical feasibility and benefit/cost ratio.

We conclude discussing the limitations of the work. One should be aware of the challenge of finding actuators capable to meet the required specification with an acceptable energy efficiency. However, the general idea we propose is valid for any skin-friction drag reduction technique, including passive strategies, e.g. riblets. Moreover, the present study is not indicative of the maximum achievable gain and a detailed investigation is deserved. Indeed, the available information for incompressible channel flow and flat boundary layers can not be scaled up straightforwardly to an airplane, where the goal is enhancing the aerodynamic efficiency and not reducing only the friction drag. It should be also considered that while the M_∞ value here considered is representative of an aircraft the Re_∞ is not. Therefore, a serious design attempt should consider larger Reynolds numbers. Luckily, we know that spanwise forcing (Gatti & Quadrio, 2016) and, more in general, skin-friction drag reduction techniques remain effective at larger Re. Nevertheless, a larger Re_∞ would lead to a different target flow that certainly requires different details in the optimisation.

REFERENCES

Albers, M. & Schröder, W. 2021 Lower drag and higher lift for turbulent airfoil flow by moving surfaces. *International Journal of Heat and Fluid Flow* **88**, 108770.

Atzori, M., Vinuesa, R., Fahland, G., Stroh, A., Gatti, D., Frohnapfel, B. & Schlatter, P. 2020 Aerodynamic Effects of Uniform Blowing and Suction on a NACA4412 Airfoil. *Flow Turbulence Combust* **105** (3), 735–759.

Banchetti, J., Luchini, P. & Quadrio, M. 2020 Turbulent drag reduction over curved walls. *J. Fluid Mech.* **896**.

Ducros, F, Ferrand, V, Nicoud, F, Weber, C, Darracq, D, Gacherieu, C & Poinsot, T 1999 Large-Eddy Simulation of the Shock/Turbulence Interaction. *Journal of Computational Physics* **152** (2), 517–549.

Gatti, D. & Quadrio, M. 2016 Reynolds-number dependence

of turbulent skin-friction drag reduction induced by spanwise forcing. *J. Fluid Mech.* **802**, 553–58.

Hosseini, S. M., Vinuesa, R., Schlatter, P., Hanifi, A. & Henningson, D. S. 2016 Direct numerical simulation of the flow around a wing section at moderate Reynolds number. *International Journal of Heat and Fluid Flow* **61**, 117–128.

Kornilov, V. 2021 Combined Blowing/Suction Flow Control on Low-Speed Airfoils. *Flow Turbulence Combust* **106** (1), 81–108.

Laflin, K.R., Klausmeyer, S.M., Zickuhr, T., Vassberg, J.C., Wahls, R.A., Morrison, J.H., Brodersen, O.P., Rakowitz, M.E., Tinoco, E.N. & Godard, J.-L. 2005 Data Summary from Second AIAA Computational Fluid Dynamics Drag Prediction Workshop. *J. Aircraft* **42** (5), 1165–1178.

Mele, B., Tognaccini, R. & Catalano, P. 2016 Performance assessment of a transonic wing-body configuration with riblets installed. *J. Aircr.* **53** (1), 129–140.

Memmolo, A., Bernardini, M. & Pirozzoli, S. 2018 Scrutiny of buffet mechanisms in transonic flow. *Int. J. Numer. Methods Heat Fluid Flow* **28** (5), 1031–1046.

Nguyen, V.-T., Ricco, P. & Pironti, G. 2021 Separation drag reduction through a spanwise oscillating pressure gradient. *J. Fluid Mech.* **912**.

Poinsot, T. J & Lele, S. K 1992 Boundary conditions for direct simulations of compressible viscous flows. *J. Comp. Phys.* **101** (1), 104–129.

Quadrio, M. & Ricco, P. 2004 Critical assessment of turbulent drag reduction through spanwise wall oscillation. *J. Fluid Mech.* **521**, 251–271.

Quadrio, M., Ricco, P. & Viotti, C. 2009 Streamwise-traveling waves of spanwise wall velocity for turbulent drag reduction. *J. Fluid Mech.* **627**, 161–178.

Schlatter, P. & Örlü, R. 2012 Turbulent boundary layers at moderate Reynolds numbers: Inflow length and tripping effects. *J. Fluid Mech.* **710**, 5–34.

Skote, M. 2012 Temporal and spatial transients in turbulent boundary layer flow over an oscillating wall. *Int. J. Heat Fluid Flow* **38**, 1–12.

Yudhistira, I. & Skote, M. 2011 Direct numerical simulation of a turbulent boundary layer over an oscillating wall. *J Turbul.* **12** (9), 1–17.

Zhang, W. & Samtaney, R. 2016 Assessment of spanwise domain size effect on the transitional flow past an airfoil. *Computers and Fluids* **124**, 39–53.